

SUBSIDENCE OF THE COLLAPSED CALDERA OF MIYAKEJIMA, 2006-2011

Yosuke Aoki¹ and Emily K. Montgomery-Brown²

¹*Earthquake Research Institute, University of Tokyo, Tokyo 113-0032, Japan*

²*Department of Geosciences, University of Wisconsin-Madison, WI 53706, USA*

ABSTRACT

Ground deformation of Miyakejima, Japan, between 2006 and 2011 was investigated from Synthetic Aperture Radar images to gain insights into the mechanics of post-caldera deformation associated with the 2000 eruption. 70 and 69 interferograms were created from 22 ascending and 21 descending images, respectively, of PALSAR boarded on the ALOS satellite. Our result reveals a localized vertical subsidence of up to 150 mm/yr around the collapsed summit. The observed displacement field is well modeled by a closing sill at 0.5 km below the surface. The compaction volume is too small to be consistent with the amount of sulfur dioxide emission. The modeled sill would thus represent the compaction of the conduit column associated with the summit collapse, rather than the gas emission.

Key words: Post-caldera deformation; PALSAR; Time-series analysis.

1. INTRODUCTION

Circular collapse structures are ubiquitous at the summit of volcanoes. They are called pit craters or calderas and exist in nearly all tectonic settings. These structures are formed by the evacuation of a crustal magma chamber due to either vertical eruption or lateral intrusion.

Structure and evolution of the collapsed caldera has been well studied by analog modeling [1] and numerical modeling [2]. The collapsed caldera is generally bounded by ring faults which are inward, outward, or mixed. Analogue and numerical experiments suggest that the geometry of the ring faults primarily depends on the ratio between the radius of the caldera and the depth of the magma chamber. Insights gained by analog and numerical experiments are consistent with the field observations [3].

Notwithstanding these extensive studies, the direct observation of the caldera formation is rare simply because the occurrence of caldera formation is rare. The 2000 eruption and caldera formation at Miyakejima, Japan, is one of such rare events, from which we can gain insights into

the observational constraints of the caldera formation. Here we investigated ground deformation of Miyakejima between June 2006 and December 2009 from Synthetic Aperture Radar (SAR) images. We first generated interferograms from coherent image pairs, then applied a time-series analysis [4, 5] to derive time-dependent deformation of all available pixels. Our goal is, again, to gain more insights into the mechanics of post-caldera deformation through taking advantages of spatially dense observations. It is worth noting that there are only six continuous Global Positioning System sites, four along the coast, in Miyakejima between 2006-2009, leading to the difficulty in gaining insights into the details of the post-caldera deformation there.

2. GEOLOGICAL BACKGROUND OF MIYAKEJIMA AND ITS 2000 ERUPTION

Miyakejima is one of the arc volcanoes on the Izu-Bonin chain associated with subduction of the Pacific plate (Fig. 1). It is a basaltic-andesitic stratovolcano with a sub-circular shape with a diameter of about 13 km and a height of 1000 m above the seafloor. The main part of the edifice was formed within the last 10,000 years [6]. The largest eruption during last 10,000 years occurred 2500 years ago with a caldera formation. The caldera then was buried by subsequent summit eruptions before the caldera formation in 2000. Eruptive activity during last 600 years are characterized by quasi-periodic flank fissure eruptions with intervals of 21 to 69 years [6]. Recently, Miyakejima erupted every ~20 years in 1940, 1962, 1983, and 2000. The 2000 eruption was phenomenal in that it resulted in a collapse of the summit with a diameter of about 1.7 km and depth of about 450 m [7].

The 2000 event of Miyakejima started from a dike intrusion followed by westward migration. Mass loss by the westward magma migration resulted in a creation of the collapsed summit. Explosions at the summit and excessive degassing followed after the emergence of the summit caldera.

A series of the activity started by a seismic swarm due to a magma intrusion beneath the summit. Earthquake locations and deformation measurements indicate that the intruded magma started to migrate west-southwestward

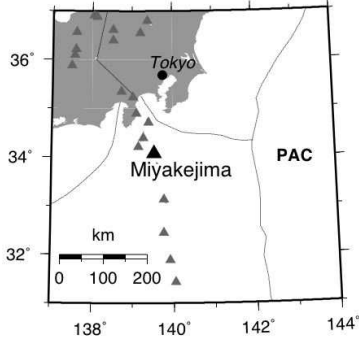


Figure 1. Location of Miyakejima denoted by a large black triangle. Smaller gray triangles represent active volcanoes. PAC denotes the Pacific plate.

in less than 12 hours after the initial intrusion [9, 10]. A submarine eruption occurred probably right after the passage of the dike [11]. Continuous GPS observations show the north-south lengthening to the west of the island due to the dike intrusion and a contraction in the island due to the outflow of magma from the island [12].

The summit collapse started on 8 July accompanied by a small explosion [13]. The collapse continued for almost two months to form a caldera with a diameter of about 1.7 km and a depth of 450 m. Tilt records during this period consist of continuous deflation and sudden inflation of the summit area, indicating that the summit did not collapse continuously with time but the collapse consists of repeating stick-slips, whereby the conduit column slips downward driven by gravitational force [14]. The summit collapse removed the load on the aquifer, leading to phreatomagmatic eruptions at the summit between 10 and 29 August [15].

Excessive degassing started after a series of phreatomagmatic eruptions, while the size of eruptions became smaller. The amount of SO_2 emission rose up to about 4×10^7 kg/day at the end of 2000 [8]. The SO_2 emission decreases gradually down to the order of 1×10^6 kg/day until 2006 and has been constant until recently.

3. DATA PROCESSING

We processed SAR images taken from PALSAR boarded on the ALOS satellite [16, 17]. PALSAR is an L-band radar, taking advantage of high coherence of interferograms even in highly vegetated areas like Miyakejima. SAR images from both the ascending and descending orbits are available. The line-of-sight (LOS) unit vectors are

$$\mathbf{e}_a = [0.6154 \quad 0.1107 \quad -0.7804]^T \quad (1)$$

for the ascending images and

$$\mathbf{e}_d = [-0.6167 \quad 0.1110 \quad -0.7793]^T \quad (2)$$

for the descending images, respectively. T denotes the matrix transpose.

The interferometric analysis was done with GAMMA software [18] for all possible pairs. The orbit of the satellite was refined with the unwrapped interferogram and Digital Elevation Model (DEM) with a resolution of 0.4 arc seconds by Geospatial Information Authority of Japan to increase the reliability in longer wavelengths. The atmospheric noise was removed with an assumption that the atmospheric effect is correlated with topography [19].

We generated 70 interferograms from 22 ascending images and 69 from 21 descending images, respectively. Note that there are many pairs whose orbital separations are too large to be coherent. Also we found that pairs with temporal baseline larger than 1.5 years tend not to be coherent enough to successfully unwrap the observed interferograms.

Fig. 2 displays an example of ascending and descending images, indicating a localized extension of the LOS distance around the summit. Qualitatively, this extension of LOS distance corresponds to subsidence rather than horizontal deformation because both ascending and descending images show the extension of LOS distance. Fig. 2 shows that the amount of LOS changes is not correlated with the baseline separation, indicating that the observed LOS changes do not purely result from DEM errors. We explore the temporal changes of the displacement more quantitatively in the next section.

4. TIME-SERIES ANALYSIS

Eqs. 1-2 shows that the observed LOS changes from both ascending and descending orbits are relatively insensitive to the north-south component so that here we estimate two components of the displacement field from the time series analysis [20].

The observed LOS changes are insensitive to the directions perpendicular to LOS vectors. As those both from ascending and descending orbits are thus insensitive to the direction

$$\mathbf{e}_p = \frac{\mathbf{e}_a \times \mathbf{e}_d}{|\mathbf{e}_a \times \mathbf{e}_d|} = [0.0002 \quad 0.9990 \quad 0.1409]^T, \quad (3)$$

we discuss the two-component displacement project onto the plane with the normal vector shown in eq. 3, which shows that the plane strikes mostly east-west and dips slightly from vertical. Here we call the two component on the plane quasi-east and quasi-vertical, the unit vectors of which are represented by

$$\mathbf{e}_{qe} = [1.0000 \quad 0.0002 \quad 0]^T \quad (4)$$

$$\begin{aligned} \mathbf{e}_{qv} &= \mathbf{e}_{qe} \times \mathbf{e}_p \\ &= [0.00003 \quad -0.1409 \quad 0.9900]^T \end{aligned} \quad (5)$$

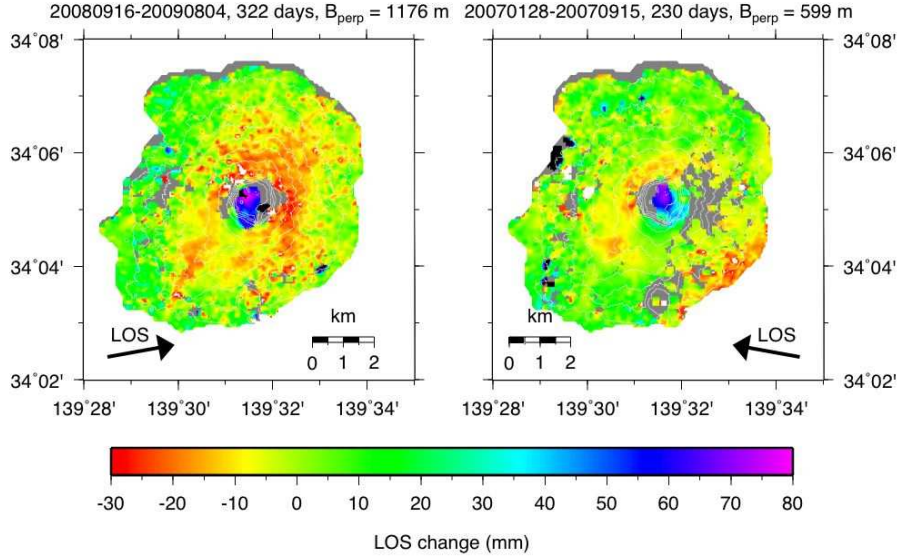


Figure 2. Sample interferograms from (left) ascending and (right) descending orbits. The left panel shows the LOS change between 16 September 2008 and 4 August 2009, a separation of 322 days. The right panel shows that between 28 January 2007 and 15 September 2007, a separation of 230 days. The perpendicular component of the orbital separation is 1176 m and 599 m. Line of sight is indicated by arrows. Solid white lines indicate contours with an interval of 100 m. Both interferograms indicate localized extension of LOS around the summit.

where e_{qe} and e_{qv} represent the unit vector for the quasi-east and quasi-vertical components, respectively.

The observed LOS changes are thus given by

$$\begin{aligned} dL_a &= (e_{qe} \cdot e_a) u_{qe} + (e_{qv} \cdot e_a) u_{qv} \\ &= 0.6154u_{qe} - 0.7882u_{qv} \end{aligned} \quad (6)$$

$$\begin{aligned} dL_d &= (e_{qe} \cdot e_d) u_{qe} + (e_{qv} \cdot e_d) u_{qv} \\ &= -0.6167u_{qe} - 0.7872u_{qv} \end{aligned} \quad (7)$$

@ where dL_a and dL_d denote LOS changes from ascending and descending orbits, respectively, and u_{qe} and u_{qv} represent the quasi-east and quasi-vertical component of the displacement, respectively.

The observation equation in our time-series analysis is given for an arbitrary pixel by

$$d_a = \sum_{i=1}^N c_i (0.6154v_{qe}^i - 0.7882v_{qv}^i) + \frac{\Delta h B_{\perp}}{\rho \sin \theta_a} \quad (8)$$

for the ascending images and

$$d_d = \sum_{i=1}^N c_i (-0.6167v_{qe}^i - 0.7872v_{qv}^i) + \frac{\Delta h B_{\perp}}{\rho \sin \theta_d} \quad (9)$$

for the descending image, respectively, where d_a and d_d represent the observed range change of ascending and descending interferograms, respectively, and v_{qe}^i and v_{qv}^i denote the quasi-east and quasi-vertical component of the velocity of the pixel. c_i denotes a fraction by which the i th time period is included in time interval corresponding to the interferogram, thus must be between 0 and 1. The

second term of eq. 8 and 9 represents the spurious signal from the DEM error, where Δh , B_{\perp} , and ρ denote the DEM error, perpendicular component of the orbital separation, and the slant range, which is about 900 km in this case. θ_a and θ_d represent the incidence angle at the pixel.

The observation equation can be written in matrix form by

$$\begin{bmatrix} d_a \\ d_d \\ 0 \\ 0 \end{bmatrix} = \begin{bmatrix} G_a^{qe} & G_a^{qv} & b_a \\ G_d^{qe} & G_d^{qv} & b_d \\ D_a/\lambda^2 & 0 & 0 \\ 0 & D_d/\lambda^2 & 0 \end{bmatrix} \begin{bmatrix} v_{qe} \\ v_{qv} \\ \Delta h \end{bmatrix} \quad (10)$$

where D_a and D represent the finite approximation of Laplacian so that so that the velocity of the pixel should be temporally smooth. λ^2 imposes the relative weight for the smoothing constraint where larger λ^2 favors a solution which fits the observation better at the expense of the roughness. Here we choose the value of λ^2 rather subjectively by visual inspection. d_a and d_d represent the observed LOS changes from ascending descending orbits, respectively, and G_a^{qe} , G_a^{qv} , G_d^{qe} , G_d^{qv} , b_a , and b_d denote the kernel corresponding to eqs. 8 and 9. v_{qe} and v_{qv} are vectors corresponding to the quasi-east and quasi-vertical component of the displacement, both of which are estimated by the inversion.

5. RESULTS

The time-series analysis reveals that the quasi-subsidence near the summit slowed down from about 150 mm/yr to

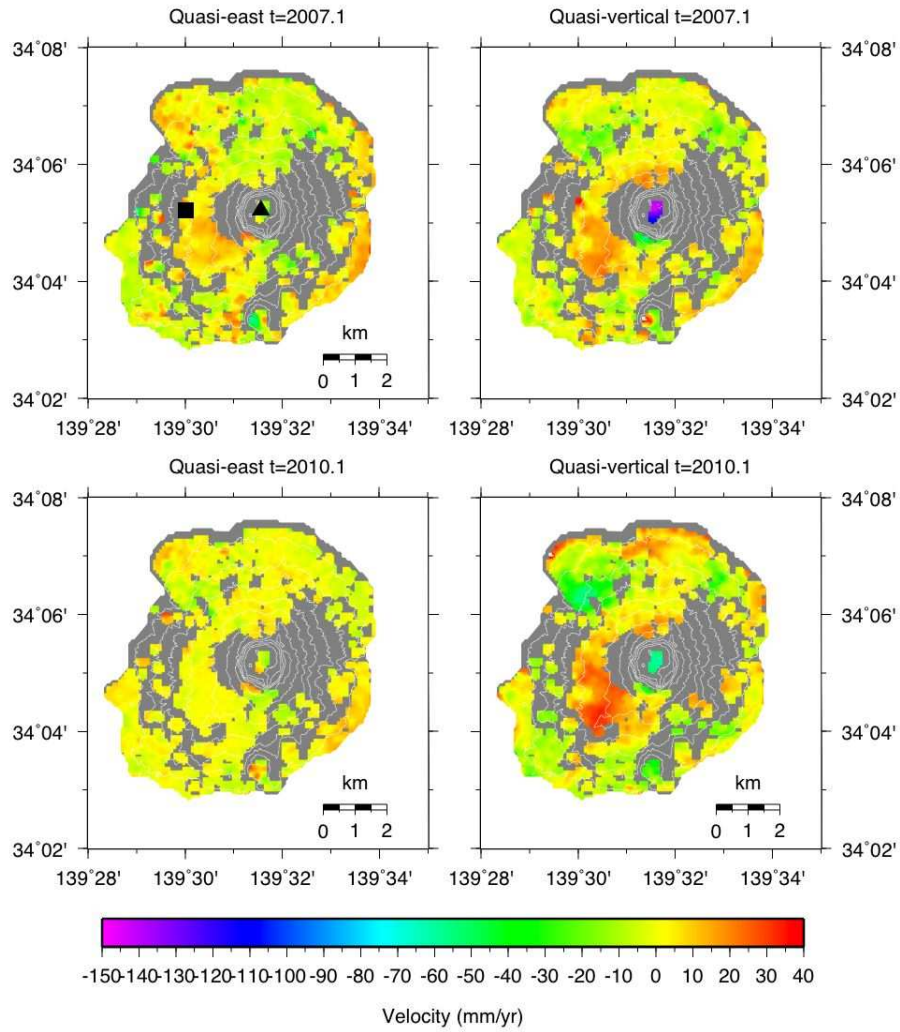


Figure 3. An example of the snapshot of the quasi-east and quasi-vertical velocities. The top panels show the quasi-east (left) and quasi-vertical (right) velocities at $t=2007.1$. The bottom panels are those at $t=2010.1$. A black triangle and rectangle indicate the location at which the temporal evolution of the velocities are shown in Fig. 4.

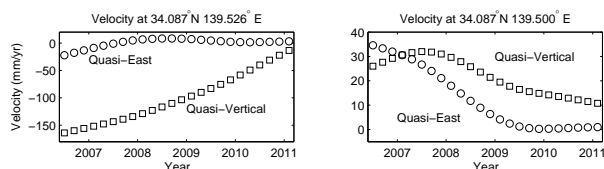


Figure 4. An example of the time series at points shown by a triangle (left) and rectangle (right) shown in Fig. 3.

50 mm/yr between 2007 and 2010 (Fig. 3). This deformation pattern is localized near the summit, implying a shallow origin of this deformation. On the other hand, southwestern part of the island exhibits the acceleration of the uplift from about 15 mm/yr in 2007 to 30 mm/yr in 2010 (Fig. 3), implying a deeper source beneath the summit. The quasi-east component of the velocity is smaller than the quasi-vertical component with a velocity only up to ~ 20 mm/yr in 2007 and less in 2010.

The temporal evolution of the deformation can be better view by looking at the time series of selected points. The left panel of Fig. 4 indicates that the subsidence near the summit slows down monotonically over time. The right panel of Fig. 4 shows that both quasi-east and quasi-vertical deformation slows down in the western flank. Note that the quasi-east velocity is much smaller than the vertical velocity. The maximum velocity of the quasi-east component is only roughly 20 % of that of the quasi-vertical component.

6. DISCUSSION

What is the likely source to cause the localized subsidence near the summit? While a spherical source is often invoked to explained the observed deformation field [21], it is not applicable in this case because the horizontal displacement is too small with respect to the vertical displacement. Note that the maximum horizontal displacement must be about 40 % of the maximum vertical displacement for a spherical source to be applicable as a viable source [21, 22]. A possible candidate is a compaction of a horizontal sill embedded at depth. A simple forward modeling with a homogeneous, elastic, and isotropic halfspace [23] suggests that a closing of a 500 m \times 500 m sill at a depth of 0.5 m below the surface can fit the observation reasonably well. However, more rigorous modeling is required for a more realistic modeling. For example, the topography must be incorporated because the deformation field due to a shallow source must be influenced by irregular topography [22, 24].

If the sill compaction is a viable source, what causes the compaction? Is the compaction caused by degassing? Consideration a sulfur concentration in the magma estimated from a melt inclusion analysis [25] shows that the magma involved in this degassing is 2 orders larger than that expected from the deformation data, indicating that the observed deformation is unrelated the degassing. In-

stead, the magma is likely to convect within the conduit where the gas emission from the magma sinks due to the negative buoyancy and the gas-rich magma is always fed from depth for the persistent degassing possible [8].

Given that the conduit has likely been fractured at the time of the caldera collapse, it is qualitatively reasonable to interpret that the observed subsidence as a result of the gravitational compaction of the conduit column. This mechanism is also consistent with the observation that the subsidence has been slowing down over time. If this mechanism is the case, a volume compaction, rather than the sill compaction, must be considered with a more sophisticated way of modeling such as Finite Element Methods.

ACKNOWLEDGMENTS

We thank Geospatial Information Authority of Japan for making their Digital Elevation Model available. PIXEL level 1.0 data from the ALOS satellite are shared among PIXEL (Palsar Interferometry Consortium to Study our Evolving Land surface) and are provided from Japan Aerospace Exploration Agency (JAXA) under a cooperative research contract with Earthquake Research Institute, University of Tokyo. The ownership of PALSAR data belongs to the Ministry of Economy, Trade, and Industry of Japan and JAXA. Some figures are created with Generic Mapping Tools [26].

REFERENCES

- [1] Acocella, V. (2007). Understanding caldera structure and development: an overview of analogue models compared to natural calderas. *Earth-Sci. Rev.* **85**, 125-160.
- [2] Hardy, S. (2008). Structural evolution of calderas: Insights from two-dimensional discrete element simulations. *Geology* **36**, 927-930.
- [3] Burchardt, S. & Walter T.R. (2010). Propagation, linkage, and interaction of caldera ring-faults: comparison between analogue experiments and caldera collapse at Miyakejima, Japan, in 2000. *Bull. Volcanol.* **72**, 297-308.
- [4] Schmidt, D.A. & Bürgmann, R. (2003). Time-dependent land uplift and subsidence in the Santa Clara valley, California, from a large interferometric synthetic aperture radar data set. *J. Geophys. Res.* **108**, 2416
- [5] Ozawa, T. & Ueda, H. (2011). New InSAR time-series analysis using interferograms of multiple-orbit paths - a case study on Miyake-jima -. *J. Geophys. Res.* submitted.
- [6] Tsukui, M. & Suzuki, Y. (1998). Eruptive history of Miyakejima volcano during the last 7000 years. *Bull. Volcanol. Soc. Jpn.* **43**, 149-166.

- [7] Geshi N., Shimano T., Chiba, T., & Nakada, S. (2002). Caldera collapse during the 2000 eruption of Miyakejima Volcano, Japan. *Bull. Volcanol.* **64**, 55-68.
- [8] Kazahaya, K. Shinohara, H., Uto, K., Odai, M., Nakahori, Y., Mori, H., Iino, H., Miyashita, M., & Hirabayashi, J. (2004). Gigantic SO₂ emission from Miyakejima volcano, Japan, caused by caldera collapse. *Geology* **32**, 425-428.
- [9] Irwan, M., Kimata, F., Fujii, N., Nakao, S., Watanabe, H., Sakai, S., Ukawa, M., Fujita, E., & Kawai, K. (2003). Rapid ground deformation of the Miyakejima volcano on 26-27 June 2000 detected by kinematic GPS analysis. *Earth Planet. Space* **55**, e13-e16.
- [10] Uhira, K., Baba, T., Mori, H., Katayama, H., & Hamada, N. (2005). Earthquake swarms preceding the 2000 eruption of Miyakejima volcano, Japan. *Bull. Volcanol.* **67**, 219-230.
- [11] Kaneko, T., Yasuda, A., Shimano, T., Nakada, S., Fujii, T., Kanazawa, T., Nishizawa, A., & Matsumoto, Y. (2005). Submarine flank eruption preceding caldera subsidence during the 2000 eruption of Miyakejima Volcano, Japan. *Bull. Volcanol.* **67**, 243-253.
- [12] Nishimura, T., Ozawa, S., Murakami, M., Sagiya, T., Tada, T., Kaidzu, M., & Ukawa, M. (2001). Crustal deformation caused by magma migration in the northern Izu islands, Japan. *Geophys. Res. Lett.* **28**, 3745-3748.
- [13] Nakada, S., Nagai, M., Kaneko, T., Nozawa, A., Suzuki-Kamata, K. (2005). Chronology and products of the 2000 eruption of Miyakejima Volcano, Japan. *Bull. Volcanol.* **67**, 205-218.
- [14] Kumagai, H., Ohminato, T., Nakano, M., Ooi, M., Kubo, A., Inoue, H., & Oikawa, J. (2001). Very-long-period seismic signals and caldera formation at Miyake island, Japan. *Science* **293**, 687-690.
- [15] Geshi, N. & Oikawa, T. (2008). Phreatomagmatic eruptions associated with the caldera collapse during the Miyakejima 2000 eruption, Japan. *J. Volcanol. Geotherm. Res.* **176**, 457-468.
- [16] Rosenqvist, A., Shimada, M., Ito, N., & Watanabe, M. (2007). ALOS PALSAR: A pathfinder mission for global-scale monitoring of the environment. *IEEE Trans. Geosci. Remote Sens.* **45**, 3307-3316.
- [17] Shimada, M., Ozawa, T., Fukushima, Y., Furuya, M., & Rosenqvist, A. (2008). Japanese L-band radar improves surface deformation monitoring. *EOS Trans. Am. Geophys. Union* **89**, 277-278.
- [18] Goldstein, R.M., & Werner, C.L. (1998). Radar interferogram filtering for geophysical applications. *Geophys. Res. Lett.* **25**, 4035-4038.
- [19] Fujiwara, S., P. Rosen, M. Tobita, & M. Murakami (1998). Crustal deformation measurements using repeat-pass JERS 1 synthetic aperture radar interferometry near the Izu Peninsula, Japan. *J. Geophys. Res.* **103**, 2411-2426.
- [20] Fujiwara, S., Nishimura, T., Murakami, M., Nakagawa, H., Tobita, M., & Rosen, P.A. (2000). 2.5-D surface deformation of M6.1 earthquake near Mt. Iwate detected by SAR interferometry. *Geophys. Res. Lett.* **27**, 2049-2052.
- [21] Mogi, K. (1958). Relations between the eruptions of various volcanoes and the deformations of the ground surface around them. *Bull. Earthq. Res. Inst. Univ. Tokyo* **36**, 99-134.
- [22] Segall, P. (2010). *Earthquake and volcano deformation*, Princeton University Press, New Jersey, USA.
- [23] Okada, Y. (1985). Surface deformation due to shear and tensile faults in a half-space. *Bull. Seismol. Soc. Am.* **75**, 1135-1154.
- [24] Williams, C.A. & Wadge, G (2000). An accurate and efficient method for including the effects of topography in three-dimensional elastic models of ground deformation with applications to radar interferometry. *J. Geophys. Res.* **105**, 8103-8120.
- [25] Saito, G., Uto, K., Kazahaya, K., Shinohara, H., Kawanabe, Y., & Satoh, H. (2005). Petrological characteristics and volatile content of magma from the 2000 eruption of Miyakejima volcano, Japan. *Bull. Volcanol.* **67**, 268-280.
- [26] Wessel, P., & Smith, W.H.F. (1998). New, improved version of the Generic Mapping Tools released. *EOS Trans. Am. Geophys. Union* **79**, 579.